THE JOURNAL OF PHYSICAL CHEMISTRY B

pubs.acs.org/JPCB Article

Variation of Energy Transfer Rates across Protein−Water Contacts with Equilibrium Structural Fluctuations of a Homodimeric Hemoglobin

Korey M. Reid, Takahisa Yamato, and David M. Leitner*

Cite This: J. Phys. Chem. B 2020, 124, 1148−1159 Read Online

ACCESS | Metrics & More | Article Recommendations | Supporting Information

ABSTRACT: Molecular dynamics simulations of the homodimeric hemoglobin from *Scapharca inaequivalvis* (HbI) have been carried out to examine relations between rates of vibrational energy transfer across nonbonded contacts and equilibrium structural fluctuations, with emphasis on protein−water contacts. The scaling of rates of energy transfer with equilibrium fluctuations of the contact length is found to hold up well for contacts between residues and hemes at the interface and the cluster of 17 interface water molecules in the unliganded state of HbI, as well as for the liganded state, for which the cluster contains on average 11 water molecules. In both states, the rate of energy transfer is also found to satisfy a diffusion relation. Within each globule, the scaling for polar contacts is similar to that found in an earlier analysis of myoglobin. Entropy associated with dynamics of polar contacts within each globule and with contacts between the hemes and water cluster is found to increase upon ligation. Energy exchange networks (EENs) for liganded and unliganded states obtained from the simulations are also presented and discussed. Energy transport networks through which nonbonded contacts transport energy in HbI, referred to as nonbonded networks (NBNs), are determined from the EENs and compared for the two states.

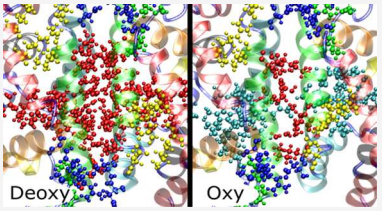

1. INTRODUCTION

Vibrational energy transport through biomolecules continues to be the focus of experimental and computational study,[1−28] with much attention given to the role of nonbonded contacts, in some cases with water molecules, in energy transport. While contacts that mediate energy transfer locally depend of course on the structures sampled by the biomolecule over times during which energy transport occurs, several studies also reveal the role of contact fluctuations in energy transfer, and a relation between rates of energy transfer and equilibrium structural fluctuations has been identified,[6,12,13] which has been studied computationally mainly for polar contacts between residues. Here, we address the relation between energy transfer across nonbonded contacts and equilibrium structural fluctuations of protein−water contacts. We carry out calculations of vibrational energy transfer in the homodimeric hemoglobin from *Scapharca inaequivalvis* (HbI), which contains a cluster of roughly 10−20 water molecules at the interface between the globules, more in the unliganded state than in the liganded. The importance of the water cluster in cooperativity has been recognized for a long time,[29−32] and its role in energy transport and the response to ligand dissociation has also been studied.[33−36] HbI serves as a good system to examine energy transfer across protein−water contacts and relations to their dynamics because the water is relatively tightly bound at the interface, compared to hydration water molecules,[34] for times that are sufficient to compute rates of energy transfer between the protein and water. We, furthermore, extend the analysis of local energy transfer to characterize networks of energy transport in this protein and examine the role of water in this process.

Energy transport in peptides and proteins is often well described by diffusive processes,[37−42] and master equation simulations adopting a Markov approximation at the length scale of residues appear to model vibrational energy transport quite well.[11,12] An interesting scaling relation between the rate of energy transfer across a nonbonded contact and equilibrium fluctuations of the contact was observed when comparing results of master equation simulations and all-atom simulations of the villin headpiece subdomain, HP36.[12] This study was carried out at low temperature, effectively below 50 K, to improve signal to noise in the energy transport data from the all-atom nonequilibrium simulations. The relation between rates of energy transfer across nonbonded contacts interacting at a short range and variance in the length of the contact was found to hold for hydrogen-bonded contacts and van der Waals interactions.[12] More recently, the relation was examined in an analysis of energy transfer within myoglobin at 300 K.[13] Despite substantially greater fluctuations in the computed rates of energy transfer at 300 K compared to the lower temperature, the proportionality of the energy transfer rate and inverse of

Received: December 10, 2019
Revised: January 20, 2020
Published: January 28, 2020

https://dx.doi.org/10.1021/acs.jpcb.9b11413
J. Phys. Chem. B 2020, 124, 1148−1159

the variance of the contact length was found to hold well for polar contacts.

We now seek to examine the extent to which this relation can be extended to biomolecule−water interactions. Calculating a rate of energy transfer is practical for contacts that survive much longer than the energy transfer time. For this reason, we start with a system where the water molecules are tightly bound to the biomolecule, more so than typical hydration water molecules,[34] and HbI satisfies this requirement. The cluster of water molecules at the interface, while mobile, rearranges on times far longer than the energy transfer times between residues and water. Hydrogen bonds between water molecules at the interface rearrange over tens of picoseconds, several times longer than hydrogen bonds between hydration water molecules, while rotational anisotropy decay for water molecules at the interface relaxes over tens to hundreds of picoseconds, an order of magnitude more slowly than for hydration water.[34] Interestingly, rotational anisotropy decay of interface water, generally slow, depends on the functional state of HbI, consistent with the results of other studies of dynamics of confined water molecules that mediate allostery, where water dynamics has also been found to depend on the functional state.[43] A depiction of HbI, highlighting the interface water and contacts at the interface, appears in Figure 1.

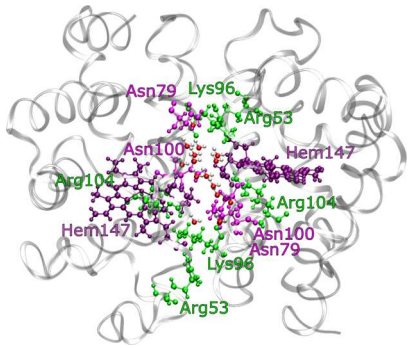

Figure 1. HbI shown in the unliganded state, where the interface water molecules and hemes and residues with which they interact are indicated.

The homodimeric hemoglobin, HbI, belongs to a large family of hemoglobins in which each globin has a fold similar to myoglobin, while the number of units and their orientation with respect to one another in the protein is diverse.[44,45] In the unliganded state of HbI, the crystal structure reveals a cluster of 17 water molecules at the interface between the two globules, whereas 11 are seen in the crystal structure of the liganded state. The free energy of ligand binding in HbI and the origin of cooperativity is largely entropic, with a substantial contribution arising from the expulsion of water molecules during ligation.[29,30,46] Important ligand-linked tertiary structural changes occur upon ligand binding, and there is a small quaternary change involving the rotation of one unit relative to the other by a few degrees.[47,48] Still, HbI exhibits cooperativity in crystals,[49−51] in which this small rotation is hindered, so that the ligand-linked tertiary changes and movement of water into and out of the interface appear sufficient for cooperativity. Prominent tertiary changes include rotation of Phe97 into the interface between the globules upon ligation, which is otherwise tightly packed against the proximal histidine, His101, in the unliganded structure. Upon ligation, rotation of Phe97 into the interface is coupled with expulsion of about 6 water molecules from the interface,[52,53] and the hemes drop toward the bottom of their respective pockets, leading to an increase in the separation of the two iron atoms from 16.6 to 18.2 Å. The cluster of water molecules at the interface, and Phe97, are integral to cooperativity. Mutations that disrupt the water cluster only at its edges, not necessarily in proximity to the hemes, alter the Hill coefficient,[29,54] as does the mutation of Phe97.[47] Time-resolved crystallographic studies following CO ligand photolysis indicate that the interfacial region, including contacts with water, are dynamically coupled to ligand dissociation, as seen in the early response to that process.[50]

Computational studies of vibrational energy transport in HbI similarly reveal dynamic coupling between the hemes and interface residues and water.[33,35,36] At early times, in response to ligand binding or dissociation, excess energy from the heme is funneled into the interface, with the cluster of water molecules mediating dynamic coupling and facilitating signaling between the globules.[33,34,55] Dynamic coupling between the hemes and residues at the interface involves both covalent and nonbonded contacts. Even neglecting covalent contacts, other than between the heme and His101, rapid energy transport between the two hemes, the interface residues, and cluster of water molecules are observed in the unliganded state through a nonbonded network (NBN) that spans both globules.[36] In the liganded state, there is also strong dynamic coupling between the hemes and residues at the interface via nonbonded contacts, though in this state there is a greater role of covalent bonds between residues of the E and F helices in funneling energy into the water cluster and to the other globule. With the local energy conductivity between residue pairs and between residues and water computed in this study, we calculate energy exchange networks (EENs), as has been carried out for other proteins in the past,[7−9] and compare the results with energy transport networks computed earlier for HbI by other methods.[36] We focus in particular on the contributions of nonbonded contacts, and their formation of NBNs, in energy transport in HbI in both the unliganded and liganded states, to examine how change in the functional state affects the networks.

In the following section, we provide information about the computational methods used to compute energy conductivity, proportional to the rate of energy transfer, across nonbonded contacts and the structural fluctuations of the contacts. In Section 3, we present and discuss the results of the computational study, examining both the relation between energy conductivity across nonbonded contacts, including polar contacts within the globules and between the residues, hemes, and water, as well as energy transport networks formed by nonbonded contacts. Concluding remarks are given in Section 4.

2. COMPUTATIONAL METHODS

Initial structures for the homodimeric hemoglobin from *Scapharca inaequivalvis* (HbI) in the deoxygenated (deoxy-HbI) and oxygenated (oxy-HbI) states were taken from the PDB entries 4SDH[56] and 1HBI,[57] respectively. All waters contained in the crystallographic PDB entries were included in the initial input. The Amber force field ff14SB[58] and the TIP3P water model[59,60] were employed and simulations were carried out with the Amber16 molecular dynamics package.[61,62] To

https://dx.doi.org/10.1021/acs.jpcb.9b11413
J. Phys. Chem. B 2020, 124, 1148−1159

parameterize a heme force field, charge density calculations were carried out using Gaussian 16[63] at the B3LYP/6-311G** level of theory. The molecular electrostatic potential was calculated using the Connolly surface algorithm[64] provided in the Gaussian software package. Two-stage charge fitting was employed using Multiwfn[65] development version 3.6 to compute the atom-centered charges for each atom within the proximal histidine and the heme. The remaining parameters for the hepta and hexavalent heme were taken from the results of Cheatham and co-workers,[66] excluding the nitrogen−iron force constant describing the proximal histidine and heme bonds, for which the heme Fe−$His_{proximal}$ N equilibrium bond length was assumed to be equal to that of the respective crystal structures for the oxy and deoxy heme. The prolines at position 1 of the primary sequence were included by prediction using UCSF Chimera's, version 1.13.1,[67] Modeller GUI interface and version 9.21 of Modeller.[68] The two systems were solvated with a buffer radius of 1.2 nm and neutralized with NaCl to a final concentration of 0.15 M. Each system was minimized for 5000 steps total to remove steric clashes, the first 500 steps of the steepest decent and the remaining steps with the conjugate gradient. The system was then heated from 0.1 K under constant volume and constant temperature (*NVT*) over 1 ns and allowed to equilibrate at 300 K for an additional 1 ns with a Langevin thermostat and a temperature time constant of 1 ps. Following *NVT* equilibration, the system was equilibrated under isothermal−isobaric conditions (*NPT*) with a Berendsen barostat[69] and a coupling constant of 2 ps for 2 ns. Following these equilibration steps, an *NPT* sampling simulation was performed for 10 ns saving velocities and coordinates every 100 ps. This totaled to 100 snapshots for each system, which were then used as the starting input for 150 ps microcanonical simulations, where the trajectory was integrated every 0.5 fs and saved every 1 fs for the velocities and 5 fs for the coordinates. An Ewald sum tolerance of 10^{-7} was employed to reduce drift.

From the final microcanonical trajectories, the midpoint theorem was applied to each velocity trajectory to calculate the velocities corresponding to the coordinate time, resulting in velocity and position trajectories with the same time per frame and 30,000 frames in total. The residue−residue currents were then calculated using CURrent calculations for Proteins.[7,8,10,70] Initially, all waters were independently included, however, this results in a large increase of noise per water−residue interaction. Upon investigation it became clear that even though the waters are stable within the interface the translational dynamics of these trapped waters, such as two or more waters exchanging position within the interface (more common) or waters hopping to the other side of the interface and back (less common) results in poor convergence of the auto-correlation function for most waters; this was exemplified in oxy-HbI, where the interfacial waters (IWs) appear less tightly bound than in deoxy-HbI. Thus, the IWs were evaluated as a single group in the interface, 17 and 11 for the deoxy- and oxy-HbI, respectively. All non-IWs were stripped from the system and not included in the analysis. The residue−residue and residue−IW currents were determined by calculating the atom−atom energy flow[8]

$$J^k_{i\leftarrow j} = \frac{1}{2}(v_i \cdot F_{ij} - v_j \cdot F_{ji}) \tag{1}$$

where $J^k_{i\leftarrow j}$ is the inter-residue atom−atom energy flow between atoms i and j for trajectory k, v is the velocity, and F is the force of one atom on the other. The inter-residue energy flow is then calculated as[8]

$$J^k_{A\leftarrow B}(t) = \sum_{i\in A}^{N_A}\sum_{j\in B}^{N_B} J^k_{i\leftarrow j}(t) \tag{2}$$

where, N_A and N_B are the number of atoms in the residue (or IW) for residue A and B. Lastly, to determine the energy currents, L_{AB}, for each pair of residues and residues with IW, we chose an ACF window of 15 ps or 3000 frames out of 150 ps (or 30,000 frames) by evaluating the following expression as a sum[8]

$$L^k_{AB} = \frac{1}{RT}\lim_{\tau\to\infty}\int_0^\tau \langle J^k_{A\leftarrow B}(t_0) J^k_{A\leftarrow B}(t + t_0)\rangle \mathrm{d}t \tag{3}$$

where R and T are, respectively, the gas constant and the temperature of the simulation. In the calculations that follow, we multiply the inter-residue energy conductivity, L_{AB}, by RT and report values in $(\text{kcal mol}^{-1})^2/\text{ps}$, a quantity referred to as G_{AB}, where$G_{AB} = (RT)L_{AB}$. We drop the subscripts AB in the following. For a residue with excess energy, the energy conductivity quantifies the net energy transferred across a nonbonded contact per unit time, and is proportional to the rate constant for energy transfer across the contact, which has been computed in other studies of energy transport in proteins.[11,12,36]

From the 100 calculations of the energy conductivity between residue pairs, we took an ensemble average of each residue−residue conductivity to produce EENs and subsequently difference in EENs (ΔEENs), where the difference refers to a change in the network when the protein changes state from unliganded to liganded.[8,9]

The central focus of this study is examination of the relation between G, which is proportional to the rate of energy transfer across a nonbonded contact, and equilibrium fluctuations in the length of the contact. We recently studied this relation computationally for myoglobin,[13] and here extend the study to include residue−water interactions, specifically residue−IW contacts. For this study, the variance in contact distance of each hydrogen-bonded pair between the donor hydrogen and acceptor oxygen is calculated for each of the 100 microcanonical simulations and the resulting variance and current for each hydrogen-bonded contact are paired. Polar contacts were defined as X−H···O, where X was taken to be either N or O and the H···O separation is no greater than 2.8 Å. We also apply a threshold of 50 $(\text{kcal mol}^{-1})^2/\text{ps}$ to enhance signal to noise. Hydrogen bonds, a sub-class of polar contacts, were selected for angles XHO ≥ 150°. Hydrogen-bonded contacts are included in the set only when the existence of a hydrogen bond exceeds 99% of the simulation time. Almost all the data computed for polar contacts correspond to hydrogen bonds, and we refer to them interchangeably. From the average distance between the O and H involved in the polar contact, r, the variance in the distance, $\langle \delta r^2\rangle = \langle (r - r)^2\rangle$, is calculated and paired with the respective G computed for this trajectory.

We briefly summarize the expectation that G and $\langle \delta r^2\rangle^{-1}$ are proportional, using a harmonic argument that has been detailed elsewhere.[6,13] The equation of motion for lattice vibrations is $m_A(\mathrm{d}^2u_A/\mathrm{d}t^2) = \sum_{A'\neq A} f_{AA'}u_{A'}$, where m_A and u_A are the mass and displacement, respectively, at site A, and $f_{AA'}$ is the force constant for the interactions connecting the masses. This equation has the same form as a master equation that describes energy transfer between residue pairs, and the water

https://dx.doi.org/10.1021/acs.jpcb.9b11413
J. Phys. Chem. B 2020, 124, 1148−1159

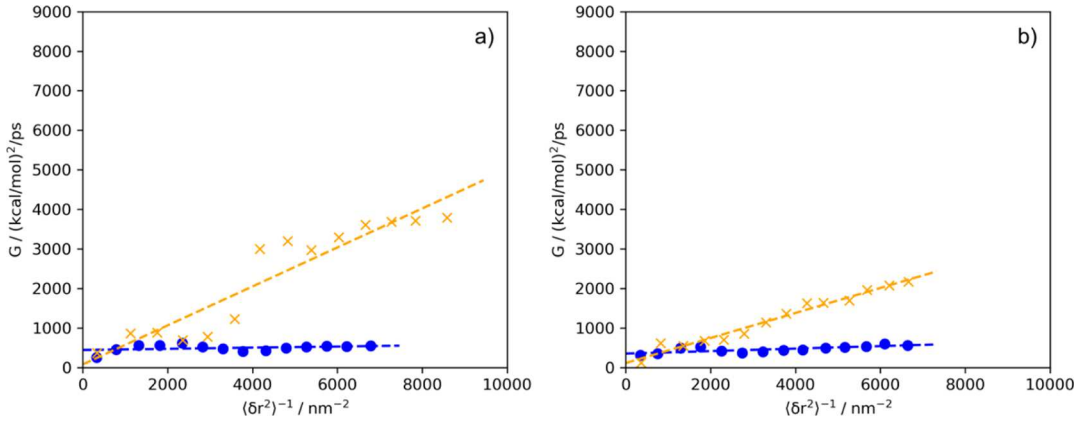

Figure 2. G vs $\langle \delta r^2 \rangle^{-1}$ for polar contacts of HbI, where results for the unliganded state are plotted in (a) and results for the oxy state in (b). Only intraglobule contacts are considered, and the data, plotted as blue and orange points, appear to lie along two lines. Best linear fits are indicated with corresponding colors.

cluster and hemes, in the protein, $dE_A/dt = \sum_{A' \neq A} w_{AA'} E_{A'} - w_{A'A} E_A$, where E_A is the energy of residue A and $w_{AA'}$ a rate constant between A and A', proportional to G. The equations differ by the presence of the first and second order time-derivatives in the master equation and the equation of motion for lattice vibrations, respectively, and some solutions to the master equation can be obtained from solutions to the vibrational dynamics by substituting t for ω^{-2}.[71−74] The interchangeability of t^{-1} and ω^2 has been observed in earlier studies of vibrational dynamics and energy flow in proteins.[4,75−77] For an oscillator $\omega^2 \propto \langle \delta r^2 \rangle^{-1}$, so that for a rate, $G \propto \langle \delta r^2 \rangle^{-1}$ after making the ω^2 to t^{-1} substitution. Of course, the actual dynamics of the protein is not harmonic. Values of G and $\langle \delta r^2 \rangle^{-1}$ that are computed for HbI from the MD simulations incorporate the full anharmonicity, and serve as an important check as to whether or not we can conclude that G and $\langle \delta r^2 \rangle^{-1}$ are indeed proportional.

3. RESULTS AND DISCUSSION

3.1. Rates of Energy Transfer across Nonbonded Contacts and Equilibrium Fluctuations. We consider here the relation between G and the inverse of the variance in the length of polar contacts, $\langle \delta r^2 \rangle^{-1}$, between residues of HbI and between residues and the cluster of water molecules at the interface in both the unliganded and liganded states. Contacts are only considered within a restricted length (2.8 Å, as-described above), and the relation is only calculated for contacts meeting this criterion for essentially the length of the trajectory over which it is computed (Section 2). During the course of the simulations, the protein may assume structures in which a particular contact is intact, others in which it is not. The rate of energy transfer across the contact is a weighted average over the rate of all of these structures, roughly the product of the rate across the intact contact and the fraction of time it is intact. We consider here only the rate for the intact contact to examine its relation to fluctuations of the contact length. We turn first to results for contacts between residues, which are shown in Figure 2.

The observed hydrogen bond contacts between residue pairs within each globule appear to fall along two lines when G is plotted against $\langle \delta r^2 \rangle^{-1}$ in both states. The specific contacts that fall on the orange and blue lines are detailed in Table S1, and Figure S7 depicts the location of the residues (see Supporting Information). The data plotted in Figure 2 are the average G for each $\langle \delta r^2 \rangle^{-1}$ indicated using the full set of data points plotted in the Supporting Information, as was done in an earlier study of myoglobin.[13] From the observed locations of donor−acceptor contact interactions between two residues, we see a similar trend to that found for short-range, polar contacts of myoglobin,[13] specifically a mixture of side chain-side chain and side chain-backbone interactions in both curves. The contacts closely match those reported for the myoglobin analysis with the exception of Asn−Asn and Arg−Met, which were not found for myoglobin.

For the blue curves, the linear equation describing the trends of G in (kcal mol^{-1})^2/ps and $\langle \delta r^2 \rangle^{-1}$ in nm^{-2} are $G = 0.015\langle \delta r^2 \rangle^{-1} + 444.0$ and $G = 0.031\langle \delta r^2 \rangle^{-1} + 352.3$, for deoxy- and oxy-HbI, respectively. For the orange curves, $G = 0.49\langle \delta r^2 \rangle^{-1} + 79.6$ and $G = 0.32\langle \delta r^2 \rangle^{-1} + 113.1$, for deoxy- and oxy-HbI, respectively. We note that the data reported here sample higher conductivities for each residue pair when compared to our prior report on myoglobin,[13] which is a result of better convergence of the autocorrelation function (eq 3) because we opted to save the velocity and coordinates with greater frequency, 5 fs instead of 10 fs, as we had previously.

As we see in Figure 2, the scaling relation between G and $\langle \delta r^2 \rangle^{-1}$ for each state exhibits a trend similar to that for myoglobin, where the data for the polar contacts fall along two lines. For HbI, we observe upon ligation an increase in the slope for the blue curve from 0.015 to 0.031 (kcal mol^{-1})^2 ps^{-1} nm^2 and decrease in slope for the orange curve from 0.49 to 0.32 (kcal mol^{-1})^2 ps^{-1} nm^2. In both cases, the slopes lie within the margin of error of each other, due to noise in the data giving rise to large fluctuations in the computed values of G around a given $\langle \delta r^2 \rangle^{-1}$, as seen in the raw data plots in the Supporting Information. In particular, for the data plotted in orange, with larger G, the slopes of the linear fits are estimated to within ±0.14 (kcal mol^{-1})^2 ps^{-1} nm^2 as a result of the fluctuations in G, so that within this error the slopes corresponding to the unliganded and liganded states are essentially the same. We also cannot rule out some contribution, albeit probably small, from collective vibrations of the protein in the difference between the slopes. A larger effective rate of energy transfer locally, across a given contact pair, may reflect to some extent the overall more rapid energy flow in the larger, unliganded protein system, which arises from the more sizable water cluster, which overall facilitates energy transport, as found in earlier simulation studies.[33−35] Never-

https://dx.doi.org/10.1021/acs.jpcb.9b11413
J. Phys. Chem. B 2020, 124, 1148−1159

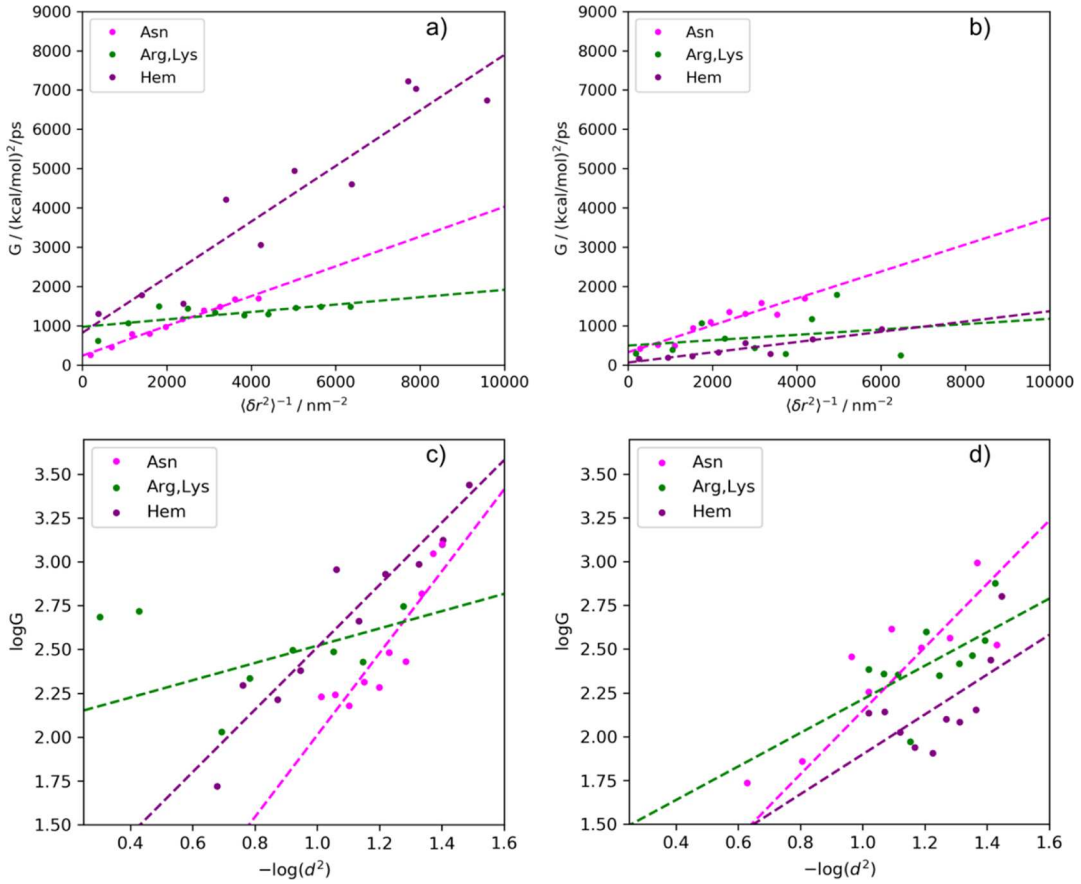

Figure 3. G vs $\langle \delta r^2 \rangle^{-1}$ for protein−water contacts of (a) unliganded and (b) liganded states of HbI. Heme−water contacts are plotted in purple, Asn−water in magenta and Lys−water and Arg−water data have been combined and plotted in green. log G vs $-\log(d^2)$ for protein−water contacts of (c) unliganded and (d) liganded states of HbI.

theless, because of significant fluctuations in the computed values of G around a given $\langle \delta r^2 \rangle^{-1}$, we expect a difference in the slope commensurate with the values found for the linear fits to the data for the unliganded and liganded states.

Also noteworthy is the difference in the range of $\langle \delta r^2 \rangle^{-1}$ for the liganded and unliganded states. That is clearly evident for the set of data plotted in orange, which have larger G. There, we see that $\langle \delta r^2 \rangle^{-1}$ extends out 28% farther for the deoxy state than the oxy state. This is consistent with a liganded state that exhibits greater flexibility than the unliganded state, as seen in previous MD simulation studies.[46] Based on those simulations an estimate of $T\Delta S \approx 1.8$ kcal mol^{-1} upon ligation was obtained at 300 K because of the contribution of greater protein flexibility, mainly along the backbone. This study noted that there may be other factors, besides the loss of water molecules, that contribute to the free energy change upon ligation.

We pointed out previously that $T\Delta S$ associated with each contact can be estimated by the change in G, or $\langle \delta r^2 \rangle^{-1}$, for the contact going from one functional state to another. Specifically, for each contact, we would expect for $\Delta S = S_L - S_U$, where S_L (S_U) refers to the entropy associated with the dynamics of a particular contact pair in the liganded (unliganded) state[6,13]

$$\Delta S = \frac{k_B}{2} \ln\left(\frac{G_U}{G_L}\right) = \frac{k_B}{2} \ln\left(\frac{\langle \delta r^2 \rangle_L}{\langle \delta r^2 \rangle_U}\right) \quad (4)$$

If, for each contact sampled, there is a 28% increase in $\langle \delta r^2 \rangle$ upon ligation that would correspond to $T\Delta S \approx 0.074$ kcal mol^{-1} for that contact at 300 K. For the 6 contacts sampled, this leads to an estimate of $T\Delta S \approx 0.44$ kcal mol^{-1}. We assume for this estimate that these contacts remain intact for the structures sampled, which is supported by the results of the simulations, where we find all 6 contacts intact for on average 93% of the entire simulation in both liganded and unliganded states. The result is about a quarter of the estimate of the contribution to the entropy change resulting from an increase in backbone flexibility and illustrates the variety of contributions to the change in entropy upon ligation.

We turn now to contacts between the IW cluster and the hemes and residues at the interface. In Figure 3a,b, we plot G versus $\langle \delta r^2 \rangle^{-1}$, which contains IW−residue interactions for three groups: (1) Asn−IW, (2) Arg−IW and Lys−IW, and (3) heme−IW. While this in fact constitutes four groups, the Arg−IW and Lys−IW data lie close to each other, so we combine them to improve statistics. This facilitates analysis of the liganded state, in particular, which has fewer such contacts and otherwise poorer statistics than for the unliganded state. The hydrogen bond contact linear fit for deoxy-HbI's Asn−IW (magenta), Arg−IW and Lys−IW (green), and heme−IW (purple) are, for G in (kcal mol^{-1})^2/ps and $\langle \delta r^2 \rangle^{-1}$ in nm^{-2}, $G = 0.38\langle \delta r^2 \rangle^{-1} + 238.4$, $G = 0.09\langle \delta r^2 \rangle^{-1} + 971.7$ and $G = 0.71\langle \delta r^2 \rangle^{-1} + 821.2$, respectively. In each case, the data follow the linear fit well. For oxy-HbI, the hydrogen bond contact linear fits are $G = 0.34\langle \delta r^2 \rangle^{-1} + 326.6$, $G = 0.07\langle \delta r^2 \rangle^{-1} + 496.4$, and $G = 0.13\langle \delta r^2 \rangle^{-1} + 63.0$ for the Asn−IW (magenta), Arg−IW and Lys−IW (green), and the heme−IW (purple),

https://dx.doi.org/10.1021/acs.jpcb.9b11413
J. Phys. Chem. B 2020, 124, 1148−1159

respectively. For the liganded system, with fewer water molecules, the data also follow the linear fit quite well, but there appear to be more fluctuations than for the unliganded system with more water molecules, particularly for Arg−IW and Lys−IW. These polar contacts, between an interfacial residue group and the water at the interface, can show striking effects because of ligation. We see that the non-heme residue−IW contacts have similar slopes for the two states, while the heme−IW slopes differ substantially between them. The propionate groups of each heme offer up to four sites for a water molecule to interact with the heme, so that for a given fluctuation in the length of a polar contact between a water molecule and the heme, G will depend on the number of water molecules in contact with the heme at a given time. For the unliganded state, the water cluster is larger and there are more simultaneous interactions between the water cluster and a heme than in the liganded state, for the trajectories sampled in this study about half a water on average more at any one time (Figure S8), yielding larger G for a given fluctuation at each contact, and a larger slope when G is plotted against $\langle \delta r^2 \rangle^{-1}$.

We observe in Figure 3 that $\langle \delta r^2 \rangle^{-1}$ for heme−IW spans a wider range in the unliganded state than in the liganded, while for the other contacts with IW the range is similar for the two states. Thus, for heme−IW there is a greater fluctuation on average in the length of the contact in the liganded state than in the unliganded state and we can expect an increase in entropy upon ligation because of enhanced fluctuations of the heme−IW contacts. This increase in entropy is quite separate, of course, from the increase in entropy because of water molecules leaving the interface upon ligation. Instead, there is an increase in entropy because of enhanced fluctuations of contacts between the hemes and the cluster of water molecules (IW) at the interface, where we take the water cluster as a single entity, that is, we neglect contributions to the entropy of internal motion of the water molecules within the cluster, which of course could also contribute. More specifically, we observe a 60% increase in $\langle \delta r^2 \rangle$ upon ligation for the heme−IW contacts, which, using eq 4, corresponds to $T\Delta S \approx 0.14$ kcal mol^{-1} for heme−water contacts at 300 K. This contribution can be added to $T\Delta S \approx 0.44$ kcal mol^{-1} already found for the greater flexibility of some of the polar contacts between residues of HbI upon ligation. We thereby find that changes in the internal dynamics, both within the globules and between the globules and the cluster of water molecules at the interface, upon change in the functional state contribute significantly to the entropy and free energy change upon ligation.

We have thus far examined the dependence of energy transfer rates with fluctuations in the contact length for contacts restricted to short distances. If we do not restrict the distance in the contact, it is also of interest to examine the distance dependence. Energy transfer in proteins is expected to exhibit diffusive dynamics, as seen in many simulations of energy flow in proteins and peptide systems noted above. Diffusive dynamics was observed for energy transfer in myoglobin between ionic contacts, where more than two charged residues mutually interact over a short distance, contacts for which the scaling of energy transfer rate with fluctuation in length over a short range may not hold.[13] We thus examine here whether the rates of energy transfer across nonbonded contacts at the interface, which are proportional to G, also follow a diffusion relation. We thus also consider the distance dependence of the contacts on G. If the rate of energy transfer satisfies a diffusion equation, the rate varies inversely with the contact distance, d, as d^{-2}. More generally, because there may be several simultaneous contacts, particularly over longer distances, we could expect a more general relation,[13] where G is proportional to d^{-2b}, in which case $b = 1$ for normal diffusion, but in general b may not be 1. We would thus generally expect that log G is proportional to $\log(1/\langle d^2 \rangle)$, where b is the slope. We, therefore, consider how log G varies with $\log(1/\langle d^2 \rangle)$, where $\langle d^2 \rangle$ is the average of the square distance between the atoms forming the contact computed over the same time interval in which G is computed.

We plot $\log(G)$ versus $-\log\langle d^2 \rangle$ in Figure 3c,d for deoxy-HbI and oxy-HbI, respectively. (We refer to $\langle d^2 \rangle$ as simply d^2 in the plots and what follows.) While for $\langle \delta r^2 \rangle^{-1}$, we applied an average distance cutoff of 0.28 nm between the donor hydrogen and the acceptor oxygen to select for hydrogen-bonded contacts, as well as a threshold of 50 (kcal mol^{-1})^2/ps, for the plots of $\log(G)$ versus $-\log d^2$, we adopt the same threshold for G, but allow any distance, d, between the contacts. We plot $\log(G)$ versus $-\log d^2$ for the Asn−IW contacts (magenta), Arg, and Lys−water contacts (green), and the heme−water contacts (purple) for the deoxy state in Figure 3c, and in Figure 3d for the oxy state. For the magenta curves, Asn−IW, the linear fit for G in (kcal mol^{-1})^2/ps and d^{-2} in nm^{-2} is $\log G = -2.34 \log d^2 - 0.33$ and $\log G = -1.81 \log d^2 + 0.33$ for deoxy- and oxy-HbI, respectively. For the green curves, Arg−IW and Lys−IW, the linear fit is $\log G = -0.49 \log d^2 + 2.03$ and $\log G = -0.96 \log d^2 + 1.25$ for deoxy- and oxy-HbI, respectively. The linear fits for the purple curves, heme−IW, are $\log G = -1.78 \log d^2 + 0.73$ and $\log G = -1.14 \log d^2 + 0.76$ for deoxy- and oxy-HbI, respectively. We note that for heme−IW, the slope, b, is close to 1 for the liganded state, but corresponds to larger b, where $b > 1$, for the unliganded state. We expect $b > 1$ when there are more than two mutually interacting groups, as we found in the myoglobin study.[13] This occurs for heme−IW in the unliganded state because of interactions between the propionate groups and the water molecules in the cluster, as noted earlier. On average, there is an additional half a water molecule in contact with one heme in the unliganded state compared to the liganded state, and for the latter it is less likely, but possible at longer distances, for there to be simultaneous interaction between one heme and more than one water molecule (Figure S8).

3.2. Energy Exchange Networks. For oxy- and deoxy-HbI, we have computed the statistical average of the energy conductivities. From this data, we produce an EEN for each system, which maps the average energy conductivity for each contact pair, and a difference EEN (ΔEEN) of the two systems, subtracting the average energy conductivity between residue pairs of the deoxy system from the energy conductivity of the residue pairs of the oxy system. As a result, our ΔEEN reveals changes in energy transport pathways via nonbonded interactions that are both intraglobule and interglobule, where the latter includes changes between IWs and the interfacial residues and the heme of each globule. The waters at the interface are grouped as one unit to overcome noise because of translational motion of individual water molecules within the interface. For instance, two water molecules are able to exchange position over the 150 ps simulation during which one value of G is computed all the while residing in the interface and ultimately interacting with the same interfacial residues when grouped. Therefore, the IWs are presented as residue Wat300 in the EENs plotted in Figure 4. There are 294

https://dx.doi.org/10.1021/acs.jpcb.9b11413
J. Phys. Chem. B 2020, 124, 1148−1159

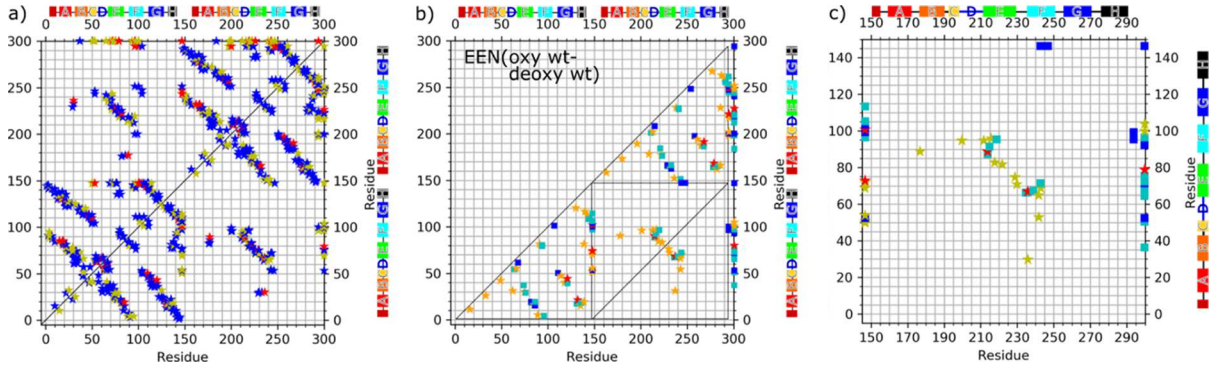

Figure 4. (a) EEN for the unliganded (above diagonal) and liganded (below diagonal) states of HbI, where the data points signify individual energy conductivities for the corresponding residue−residue pair. The residue numbers are listed on the vertical and horizontal axes, and helical regions are indicated with different colors as an aid (the unlabeled dark red refers to the pre-A helix). The water cluster is in position 300. Symbols mark significant residue−residue energy conductivity, where blue corresponds to values between 10 and 100 (kcal mol^{-1})^2/ps, yellow to values between 100 and 1000 (kcal mol^{-1})^2/ps and red to values greater than 1000 (kcal mol^{-1})^2/ps. (b) Plot of ΔEEN = EEN(oxy) − EEN(deoxy). (★) Increase in energy exchange, where, yellow are changes between 50 and 500 (kcal/mol)^2/ps and red changes greater than 500 (kcal/mol)^2/ps. (■) Decrease in energy exchange, where, cyan are changes between −50 and −500 (kcal/mol)^2/ps and blue less than −500 (kcal/mol)^2/ps. (c) ΔEEN for the interface region. Table S3 lists the residue names and corresponding number of each residue.

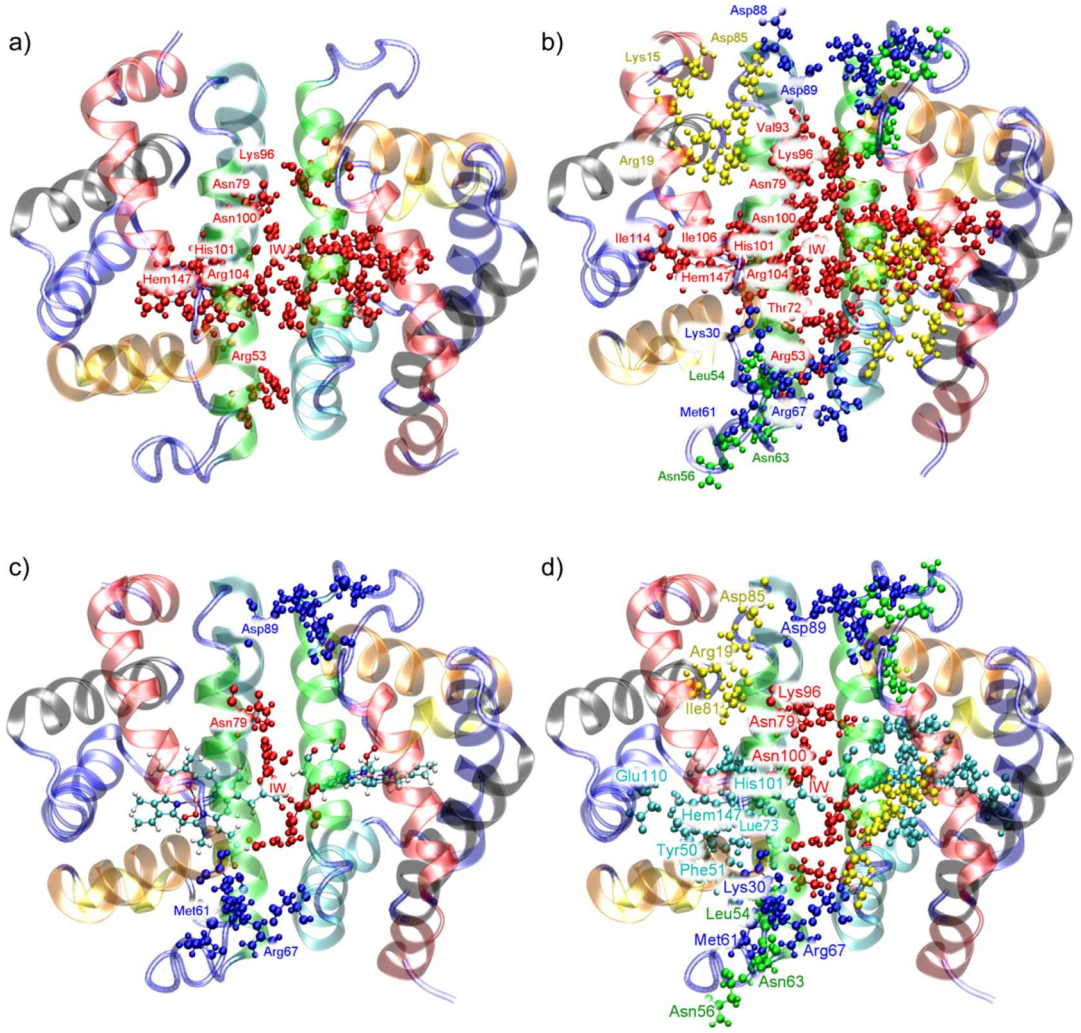

Figure 5. NBN of HbI in (a,b) unliganded state and (c,d) liganded state. The backbone structure is shown in blue tubes for the loops and in specific colors corresponding to each helix using the same color scheme as in Figure 4. Residues and water belonging to an NBN are colored by their cluster network, as discussed in the text. (a,c) correspond to an energy conductivity threshold of 1000 (kcal mol^{-1})^2/ps, whereas (b,d) correspond to a threshold of 250 (kcal mol^{-1})^2/ps. Residues are labeled and IWs are denoted by IW. Residue labels are only placed on globule A of the homodimer and color coded to the network to which they belong.

https://dx.doi.org/10.1021/acs.jpcb.9b11413
J. Phys. Chem. B 2020, 124, 1148−1159

residues including the hemes, but we include the IWs as residue 300 so that interactions with the IWs can be easily spotted. In Figure 4, we plot (a) the EEN for deoxy-HbI above the diagonal and for oxy-HbI below, (b) the ΔEEN for the protein, and (c) the ΔEEN for the interface region, which provides a close-up of changes that occur there.

From Figure 4a, we see overall striking similarities between the deoxy (upper diagonal) and the oxy (lower diagonal) states, which might be expected for a protein that undergoes only modest structural changes.[50] However, from the ΔEEN we see that a number of nonbonded contacts differ in their energy conductivity in going from the unliganded state to the liganded state, consistent with prior computational findings.[33−36] Examining the ΔEEN, plotted in Figure 4b, we see that the contacts between residues and the interface waters exhibit the largest decrease in energy conductivity upon ligation. On the other hand, the largest increases in energy conductivities are found for residue contacts across the interface. Both trends are consistent with the reduction in the number of IWs as a result of Phe97 displacing on average 6 waters upon ligation.[29] This reduction in waters at the interface results in interfacial residues losing the available network node via the waters, ultimately signaling a rise in energy conductivity elsewhere. Some intraglobule contacts also exhibit a decrease in the energy conductivity in the transition from deoxy to the oxy state, and a few appear to increase, as seen in Figure 4b. The modest net decrease in local energy conductivity between residues within the globules of HbI upon ligation is consistent with the scaling curves shown in Figure 2, where a shift to smaller $\langle \delta r^2 \rangle^{-1}$, and thus smaller G is seen in going from the deoxy to the oxy state.

Focusing on the interface, we see a reduction of energy transfer between residues and the cluster of water molecules in going from the deoxy to the oxy state, seen from the blue data points (Figure 4c) that dominate the interfacial residues−water contacts of the ΔEEN. The number of contacts that we see with a decrease in energy conductivity across the interface mediated by the water is compensated somewhat by increase in energy transfer between residues across the interface.

We can visualize the networks more easily by connecting nonbonded residue pairs that are linked by relatively large values of the energy conductivity, which we refer to as a NBN. Network analysis of proteins has provided information about regions in which residues are strongly connected, using a range of definitions of networks including geometry and interactions that give rise to dynamic coupling and energy transport.[78−87] Our focus here is on the contributions of nonbonded contacts in dynamic coupling and energy flow among a network of residues and water. The NBNs that we have identified using the local energy conductivity for the unliganded and liganded states of HbI are depicted in Figure 5 and are shown in different colors corresponding to clusters of differing size. Clusters here range from sets of 3 participant-residues per NBN, common within each panel, and some as large as 23. The NBNs displayed in Figure 5 contain two images per HbI state, with thresholds of 1000 (kcal mol^{-1})^2/ps and 250 (kcal mol^{-1})^2/ps, the former quite high, with a relatively small number of NBNs emerging, the latter lower and revealing a larger number of NBNs.

We consider first the NBNs for the unliganded and liganded states at the higher threshold, 1000 (kcal mol^{-1})^2/ps, plotted in Figure 5a,c. Deoxy-HbI has a single NBN in red at the highest threshold with contacts connecting the middle of the CD loop, the end of the E-helix, the end of the F-helix, following the F-helix at the edge of the interface and Hem147, from both globules, plus the IW. This NBN bridges the interface at three locations, one between the IW and Asn79, accounting for two locations, and between the IW and the hemes. Thus, the IWs constitute a critical junction for energy transport at the higher threshold within the deoxy system. Turning to oxy HbI at the 1000 (kcal mol^{-1})^2/ps threshold, we observe three NBNs. The first has residues that connect the middle of the E-helix of both globules via the IW in red. The second contains residues from the end of the CD loop, the beginning of the E-helix and the beginning of the F-helix of the opposing globule in blue, where the second NBN accounts for two distinct and isolated NBNs, all three of which span the interface. In contrast to deoxy HbI, oxy HbI has three distinctly isolated NBNs, with three participants each, the result of ligation and the reduction in the number of IWs displaced by Phe97. From the NBNs identified for oxy-HbI at or above 1000 (kcal mol^{-1})^2/ps, we see a reduction in the number of residues participating in unique networks of at least 3 or more, a direct consequence of displaced IWs, yielding a more fragmented NBN structure than for deoxy-HbI.

We consider now NBNs for the two HbI states at a smaller threshold, specifically 250 (kcal mol^{-1})^2/ps, plotted in Figure 5b,d. Deoxy-HbI has one NBN containing 22 residues plus the IW, two containing 5 residues, two containing 4 residues, and two containing 3 residues. The largest NBN spans the interface and constitutes interactions between the beginning of the CD loop, the middle and end of the E-helix, the middle and end of the F-helix, the beginning and end of the loop between the E and F helices, and the middle of the G-helix, along with the hemes and the IW. The NBN with residues labeled in blue spans the interface with interactions between the beginning of the B-helix, the end of the CD-loop, the beginning of the E-helix, and the F-helix of the opposing globule. The NBN depicted in yellow has residues from the middle and end of the A-helix, the end of the E-helix and a residue in the middle of the E and F-loops. Lastly, for deoxy-HbI, the green NBN includes two residues from the middle of the CD-loop and one from the end. Next, for oxy-HbI, the NBN in red includes residues from both globules at the end of the E-helix, middle and end of the F-helix and, also, the IWs. The NBN in cyan connects the end of the C-helix, the beginning of the CD-loop, the middle of the E-helix, the end of the F-helix, the beginning of the G-helix, and the heme. The last two NBNs contain three residues each. The yellow NBN connects the middle of the A-helix, the end of the E-helix, and the loop between the E and F-helices. The green NBNs have two residue contacts at the middle of the CD-loop interacting with the end of the CD-loop. The specific residues involved in each NBN at each threshold can be found in Table S2 of the Supporting Information.

The NBNs found for each threshold value of the inter-residue energy conductivity are clearly not the same for the two states of HbI. This trend was observed in a previous study, where the NBN was defined in terms of transition times between nonbonded residues separated by a distance, d, where the transition time, τ, was calculated in terms of the local energy diffusivity, D, using a diffusion relation, $\tau = d^2/2D$.[36] Similar to this study, the liganded state was found to lack a direct pathway via nonbonded contacts between the hemes over a range of τ where a direct pathway, through the water cluster, was observed for the unliganded state. There are also

https://dx.doi.org/10.1021/acs.jpcb.9b11413
J. Phys. Chem. B 2020, 124, 1148−1159

regional similarities with relation to each NBN and their specific residues found in this study and the earlier one.[36] Both studies reveal a distinct difference in NBN content for the two states at higher conductivity thresholds, where deoxy-HbI has sustained NBNs with higher conductivities compared to oxy-HbI, and oxy-HbI has a larger number of NBNs containing fewer participants at each threshold. This indicates a restructuring of the NBN participants to compensate for the diminished number of IWs in oxy-HbI. The energy pathways via nonbonded contacts across the globules become less favorable because there are fewer IWs, and the transfer of energy from the hemes into and across the interface requires more of a combination of bonded and nonbonded contacts than for the unliganded state,[36] in which energy flows more easily in this region via nonbonded contacts. Moreover, the smaller NBNs seen for oxy-HbI at each threshold are consistent with overall smaller G within the globules of the liganded state compared to the unliganded state, noted earlier, due to the increased flexibility of the globules upon ligation.

4. CONCLUSIONS

We have examined the relation between rates of vibrational energy transfer across protein−water contacts and equilibrium structural fluctuations of the homodimeric hemoglobin from *Scaphara inaequivalvis* (HbI). The interface water of HbI is tightly bound compared to hydration water, providing sufficient time for rates of energy transfer between water−protein contacts to be computed. Moreover, the globules are similar to myoglobin, so that the results obtained for polar contacts within each globule of HbI could be compared with the results for polar contacts computed previously for myoglobin.[13] Changes in entropy upon ligation associated with the changes in dynamics of polar contacts within the globules of HbI and between the hemes and the water cluster at the interface were evaluated. Energy transport pathways via nonbonded contacts obtained from the set of energy conductivity values computed for unliganded and liganded states of HbI in this study were also compared with earlier energy transport networks computed for this protein by other approaches.

Rates of vibrational energy transfer across contacts between residues and IW of HbI have been found to scale with equilibrium fluctuations in the length of contacts. In general, we expect the rate of energy transfer to vary linearly with the inverse of the variance of the contact length for a given short-range contact, and that is seen to hold well for deoxy-HbI, and reasonably well for oxy-HbI, which contains fewer water molecules. However, the slope may depend on the specific contact, and that is seen in the results here. For deoxy-HbI, heme−IW contacts exhibit strikingly large energy conductivity for a given variance in the contact distance, Lys−IW and Arg−IW exhibit similar conductivity to each other, and Asn−IW contacts exhibit an energy conductivity that increases fairly steeply with the inverse of the variance of the contact distance compared to Arg−IW and Lys−IW. For oxy-HbI, the rate of energy transfer between the heme and water cluster is generally smaller than for deoxy-HbI because of the smaller number of water−heme contacts at any one time. If the contact length is not restricted, and is instead allowed to vary beyond the region where a hydrogen bond can be defined, we also find that the energy transfer rate across the contact can be described by a diffusion equation, as seen in earlier work on myoglobin[13] for energy transfer across contacts formed by partial charges interacting over relatively long distances.

Within the globules of HbI in liganded and unliganded states, the scaling between energy transfer rates and equilibrium structural fluctuations for nearby polar contacts resembles that for myoglobin, where the contact pairs break up into two groups. Interestingly, the fluctuations in hydrogen bond length are on average greater for the liganded state than the unliganded, indicating that the globules are more flexible in the liganded state, consistent with the results of earlier MD simulations of HbI.[46] This work found an increase in $T\Delta S$ of about 1.8 kcal mol^{-1} at 300 K upon ligation because of increased backbone flexibility, a contribution to the free energy of ligation that had been mostly overlooked, compared to the well-studied contribution of the loss of water molecules from the interface. $T\Delta S$ associated with a change in contact dynamics upon ligation can be estimated in terms of the rate of energy transfer across the contact in each functional state.[6,13] Accounting for the 6 hydrogen-bonded contacts sampled where the fluctuations are on average larger in the liganded state, we estimate at 300 K an entropic contribution to the free energy of ligation for these contacts to be $T\Delta S \approx$ 0.44 kcal mol^{-1}. Fluctuations in the hydrogen bonds between the hemes and the cluster of water molecules at the interface are also greater in the liganded state than the unliganded state, providing an additional $T\Delta S \approx 0.14$ kcal mol^{-1} at 300 K upon ligation. We have thus identified contributions to the entropy change upon ligation that are due to changes in the internal dynamics, both within the globules and between the globules and the cluster of water molecules at the interface, that contribute to HbI cooperative binding, in addition to the long recognized change in free energy because of the expulsion of water molecules from the interface. Energy transfer across nonbonded contacts can be measured by time-resolved vibrational spectroscopies,[14,15,27] providing a means to detect such changes in contact dynamics with changes in the functional state.

Finally, EENs were computed for HbI in unliganded and liganded states to examine changes upon ligation. With the loss of water molecules at the interface, contacts between protein side chains and the IW diminish upon ligation and on average the energy conductivity between protein side chains and IW decreases, compensated somewhat by enhanced energy transfer across some of the side chains on each globule at the interface. From the EENs, NBNs linking residues, hemes, and water by nonbonded interactions and providing channels for energy transport via nonbonded contacts were computed. The NBNs obtained from the results of the MD simulations in this study were found to be close to those computed by a different approach in an earlier work.[36] They reveal dynamic coupling via nonbonded contacts between the ligand-binding region (the heme) and the water-binding region (the interface) in both states. Because of the smaller water cluster in the liganded state, energy transport between the two hemes is seen to be less efficient than in the unliganded state. This suggests that dynamic coupling between the hemes and the interface region in both states may be important in cooperativity, and indeed such dynamic coupling is observed on the nanosecond time scale in time-resolved crystallographic measurements following ligand photodissociation of CO−HbI.[50] While ligand binding sites of an allosteric protein need not be dynamically coupled on a vibrational time scale,[88−90] even if in some cases, vibrational energy transport channels between them have been

https://dx.doi.org/10.1021/acs.jpcb.9b11413
J. Phys. Chem. B 2020, 124, 1148−1159

identified,[91] regions that contribute to early allosteric transitions, in this case, the ligand-binding site and the interface, are dynamically coupled on fast time scales. This coupling has been seen experimentally[50] and in the vibrational energy transport networks identified here and in other studies.[35,36]

The scaling relation observed here for rates of energy transfer across protein−water contacts with equilibrium fluctuations of the contact extends the range of applicability of this relation found in an earlier work. Further analysis of weaker interactions, in particular van der Waals contacts, would be valuable, even if it is computationally more difficult to study than polar contacts because of the smaller rate of energy transfer. Numerous time-resolved spectroscopy measurements highlight the importance of energy transfer across van der Waals contacts to energy transport in proteins.[14−18,92,93]

■ ASSOCIATED CONTENT

Supporting Information

The Supporting Information is available free of charge at https://pubs.acs.org/doi/10.1021/acs.jpcb.9b11413.

Scaling figures identifying specific residue pairs with a complete set of data points, table listing residue pairs, figure illustrating the location, figure quantifying heme−water contacts and the table of residues forming NBNs, and list of residues of HbI (PDF)

■ AUTHOR INFORMATION

Corresponding Author

David M. Leitner − *Department of Chemistry, University of Nevada, Reno, Reno, Nevada 89557, United States; Graduate School of Science, Division of Material Science, Nagoya University, Nagoya 464-8602, Japan;* orcid.org/0000-0002-3105-818X; Email: dml@unr.edu

Authors

Korey M. Reid − *Department of Chemistry, University of Nevada, Reno, Reno, Nevada 89557, United States*

Takahisa Yamato − *Graduate School of Science, Division of Material Science, Nagoya University, Nagoya 464-8602, Japan;* orcid.org/0000-0002-0685-861X

Complete contact information is available at: https://pubs.acs.org/10.1021/acs.jpcb.9b11413

Notes

The authors declare no competing financial interest.

■ ACKNOWLEDGMENTS

Part of this work was carried out while D.M.L. was a JSPS Invitational Fellow at Nagoya University. Support from NSF grant CHE-1854271 (to D.M.L.) is gratefully acknowledged.

■ REFERENCES

(1) Levantino, M.; Schirò, G.; Lemke, H. T.; Cottone, G.; Glownia, J. M.; Zhu, D.; Chollet, M.; Ihee, H.; Cupane, A.; Cammarata, M. Ultrafast Myoglobin Structural Dynamics Observed with an X-Ray Free-Electron Laser. *Nat. Commun.* **2015**, *6*, 6772.

(2) Barends, T. R. M.; et al. Direct Observation of Ultrafast Collective Motions in Co Myoglobin Upon Ligand Dissociation. *Science* **2015**, *350*, 445−450.

(3) Brinkmann, L. U. L.; Hub, J. S. Ultrafast Anisotropic Protein Quake Propagation after Co Photodissociation in Myoglobin. *Proc. Natl. Acad. Sci. U.S.A.* **2016**, *113*, 10565−10570.

(4) Leitner, D. M. Energy Flow in Proteins. *Annu. Rev. Phys. Chem.* **2008**, *59*, 233−259.

(5) Leitner, D. M.; Straub, J. E. *Proteins: Energy, Heat and Signal Flow*; CRC Press, Taylor & Francis Group: Boca Raton, FL, 2010.

(6) Leitner, D. M.; Pandey, H. D.; Reid, K. M. Energy Transport across Interfaces in Biomolecular Systems. *J. Phys. Chem. B* **2019**, *123*, 9507−9524.

(7) Ishikura, T.; Yamato, T. Energy Transfer Pathways Relevant for Long-Range Intramolecular Signaling of Photosensory Protein Revealed by Microscopic Energy Conductivity Analysis. *Chem. Phys. Lett.* **2006**, *432*, 533−537.

(8) Ishikura, T.; Iwata, Y.; Hatano, T.; Yamato, T. Energy exchange network of inter-residue interactions within a thermally fluctuating protein molecule: A computational study. *J. Comput. Chem.* **2015**, *36*, 1709−1718.

(9) Ota, K.; Yamato, T. Energy Exchange Network Model Demonstrates Protein Allosteric Transition: An Application to an Oxygen Sensor Protein. *J. Phys. Chem. B* **2019**, *123*, 768−775.

(10) Leitner, D. M.; Yamato, T. Mapping Energy Transport Networks in Proteins. In *Reviews in Computational Chemistry*; Parrill, A. L., Lipkowitz, K. B., Eds.; John Wiley & Sons, Inc., 2018; Vol. *31*, pp 63−114.

(11) Leitner, D. M.; Buchenberg, S.; Brettel, P.; Stock, G. Vibrational Energy Flow in the Villin Headpiece Subdomain: Master Equation Simulations. *J. Chem. Phys.* **2015**, *142*, 075101.

(12) Buchenberg, S.; Leitner, D. M.; Stock, G. Scaling Rules for Vibrational Energy Transport in Globular Proteins. *J. Phys. Chem. Lett.* **2016**, *7*, 25−30.

(13) Reid, K. M.; Yamato, T.; Leitner, D. M. Scaling of Rates of Vibrational Energy Transfer in Proteins with Equilibrium Dynamics and Entropy. *J. Phys. Chem. B* **2018**, *122*, 9331−9339.

(14) Yamashita, S.; Mizuno, M.; Tran, D. P.; Dokainish, H.; Kitao, A.; Mizutani, Y. Vibrational Energy Transfer from Heme through Atomic Contacts in Proteins. *J. Phys. Chem. B* **2018**, *122*, 5877−5884.

(15) Mizutani, Y. Time-Resolved Resonance Raman Spectroscopy and Application to Studies on Ultrafast Protein Dynamics. *Bull. Chem. Soc. Jpn.* **2017**, *90*, 1344−1371.

(16) Kondoh, M.; Mizuno, M.; Mizutani, Y. Importance of Atomic Contacts in Vibrational Energy Flow in Proteins. *J. Phys. Chem. Lett.* **2016**, *7*, 1950−1954.

(17) Fujii, N.; Mizuno, M.; Mizutani, Y. Direct Observation of Vibrational Energy Flow in Cytochrome C. *J. Phys. Chem. B* **2011**, *115*, 13057−13064.

(18) Fujii, N.; Mizuno, M.; Ishikawa, H.; Mizutani, Y. Observing Vibrational Energy Flow in a Protein with the Spatial Resolution of a Single Amino Acid Residue. *J. Phys. Chem. Lett.* **2014**, *5*, 3269−3273.

(19) Nguyen, P. H.; Hamm, P.; Stock, G. Nonequilibrium Molecular Dynamics Simulation of Photoinduced Energy Flow in Peptides: Theory Meets Experiment. In *Proteins: Energy, Heat and Signal Flow*; Leitner, D. M., Straub, J. E., Eds.; CRC Press, Taylor & Francis Group: Boca Raton, 2010; pp 149−168.

(20) Schade, M.; Moretto, A.; Donaldson, P. M.; Toniolo, C.; Hamm, P. Vibrational Energy Transport through a Capping Layer of Appropriately Designed Peptide Helices over Gold Nanoparticles. *Nano Lett.* **2010**, *10*, 3057−3061.

(21) Nguyen, P. H.; Park, S.-M.; Stock, G. Nonequilibrium molecular dynamics simulation of the energy transport through a peptide helix. *J. Chem. Phys.* **2010**, *132*, 025102.

(22) Agbo, J. K.; Xu, Y.; Zhang, P.; Straub, J. E.; Leitner, D. M. Vibrational Energy Flow across Heme-Cytochrome C and Cytochrome C-Water Interfaces. *Theor. Chem. Acc.* **2014**, *133*, 1504.

(23) Xu, Y.; Leitner, D. M. Vibrational Energy Flow through the Green Fluorescent Protein-Water Interface: Communication Maps and Thermal Boundary Conductance. *J. Phys. Chem. B* **2014**, *118*, 7818−7826.

(24) Fujisaki, H.; Straub, J. E. Vibrational Energy Relaxation of Isotopically Labeled Amide I Modes in Cytochrome C: Theoretical Investigation of Vibrational Energy Relaxation Rates and Pathways. *J. Phys. Chem. B* **2007**, *111*, 12017−12023.
(25) Bu, L.; Straub, J. E. Simulating Vibrational Energy Flow in Proteins: Relaxation Rate and Mechanism for Heme Cooling in Cytochrome C. *J. Phys. Chem. B* **2003**, *107*, 12339−12345.
(26) Viet, M. H.; Derreumaux, P.; Li, M. S.; Roland, C.; Sagui, C.; Nguyen, P. H. Picosecond Dissociation of Amyloid Fibrils with Infrared Laser: A Nonequilibrium Simulation Study. *J. Chem. Phys.* **2015**, *143*, 155101.
(27) Baumann, T.; Hauf, M.; Schildhauer, F.; Eberl, K. B.; Durkin, P. M.; Deniz, E.; Löffler, J. G.; Acevedo-Rocha, C. G.; Jaric, J.; Martins, B. M.; et al. Site-Resolved Observation of Vibrational Energy Transfer Using a Genetically Encoded Ultrafast Heater. *Angew. Chem., Int. Ed.* **2019**, *58*, 2899−2903.
(28) Elenewski, J. E.; Velizhanin, K. A.; Zwolak, M. Topology, Landscapes and Biomolecular Energy Transport. *Nat. Commun.* **2019**, *10*, 4662.
(29) Royer, W. E.; Pardanani, A.; Gibson, Q. H.; Peterson, E. S.; Friedman, J. M. Ordered Water Molecules as Key Allosteric Mediators in a Cooperative Dimeric Hemoglobin. *Proc. Natl. Acad. Sci. U.S.A.* **1996**, *93*, 14526−14531.
(30) Ikeda-Saito, M.; Yonetani, T.; Chiancone, E.; Ascoli, F.; Verzili, D.; Antonini, E. Thermodynamic properties of oxygen equilibria of dimeric and tetrameric hemoglobins from Scapharca inaequivalvis. *J. Mol. Biol.* **1983**, *170*, 1009−1018.
(31) Cui, Q.; Karplus, M. Allostery and Cooperativity Revisited. *Protein Sci.* **2008**, *17*, 1295−1307.
(32) Boffi, A.; Chiancone, E. Evaluating Cooperativity in Dimeric Hemoglobins. *Methods Enzymol.* **2004**, *379*, 55−64.
(33) Agbo, J. K.; Gnanasekaran, R.; Leitner, D. M. Communication Maps: Exploring Energy Transport through Proteins and Water. *Isr. J. Chem.* **2014**, *54*, 1065−1073.
(34) Gnanasekaran, R.; Xu, Y.; Leitner, D. M. Dynamics of Water Clusters Confined in Proteins: A Molecular Dynamics Simulation Study of Interfacial Waters in a Dimeric Hemoglobin. *J. Phys. Chem. B* **2010**, *114*, 16989−16996.
(35) Gnanasekaran, R.; Agbo, J. K.; Leitner, D. M. Communication Maps Computed for Homodimeric Hemoglobin: Computational Study of Water-Mediated Energy Transport in Proteins. *J. Chem. Phys.* **2011**, *135*, 065103.
(36) Leitner, D. M. Water-Mediated Energy Dynamics in a Homodimeric Hemoglobin. *J. Phys. Chem. B* **2016**, *120*, 4019−4027.
(37) Schade, M.; Hamm, P. Transition from Ivr Limited Vibrational Energy Transport to Bulk Heat Transport. *Chem. Phys.* **2012**, *393*, 46−50.
(38) Botan, V.; Backus, E. H. G.; Pfister, R.; Moretto, A.; Crisma, M.; Toniolo, C.; Nguyen, P. H.; Stock, G.; Hamm, P. Energy Transport in Peptide Helices. *Proc. Natl. Acad. Sci. U.S.A.* **2007**, *104*, 12749−12754.
(39) Backus, E. H. G.; Nguyen, P. H.; Botan, V.; Pfister, R.; Moretto, A.; Crisma, M.; Toniolo, C.; Stock, G.; Hamm, P. Energy Transport in Peptide Helices: A Comparison between High- and Low-Energy Excitations. *J. Phys. Chem. B* **2008**, *112*, 9091−9099.
(40) Yu, X.; Leitner, D. M. Vibrational Energy Transfer and Heat Conduction in a Protein. *J. Phys. Chem. B* **2003**, *107*, 1698−1707.
(41) Yu, X.; Leitner, D. M. Heat Flow in Proteins: Computation of Thermal Transport Coefficients. *J. Chem. Phys.* **2005**, *122*, 054902.
(42) Leitner, D. M. Heat Transport in Molecules and Reaction Kinetics: The Role of Quantum Energy Flow and Localization. *Adv. Chem. Phys.* **2005**, *130*, 205−256.
(43) Lee, Y.; Kim, S.; Choi, S.; Hyeon, C. Ultraslow Water-Mediated Transmembrane Interactions Regulate the Activation of A2A Adenosine Receptor. *Biophys. J.* **2016**, *111*, 1180−1191.
(44) Royer, W. E.; Knapp, J. E.; Strand, K.; Heaslet, H. A. Cooperative Hemoglobins: Conserved Fold, Diverse Quaternary Assemblies and Allosteric Mechanisms. *Trends Biochem. Sci.* **2001**, *26*, 297−304.
(45) Royer, W. E.; Zhu, H.; Gorr, T. A.; Flores, J. F.; Knapp, J. E. Allosteric Hemoglobin Assembly: Diversity and Similarity. *J. Biol. Chem.* **2005**, *280*, 27477−27480.
(46) Laine, J. M.; Amat, M.; Morgan, B. R.; Royer, W. E.; Massi, F. Insight into the Allosteric Mechanism of Scapharca Dimeric Hemoglobin. *Biochem* **2014**, *53*, 7199−7210.
(47) Kim, K. H.; et al. Direct Observation of Cooperative Protein Structural Dynamics of Homodimeric Hemoglobin from 100 Ps to 10 Ms with Pump−Probe X-Ray Solution Scattering. *J. Am. Chem. Soc.* **2012**, *134*, 7001−7008.
(48) Kim, J. G.; Muniyappan, S.; Oang, K. Y.; Kim, T. W.; Yang, C.; Kim, K. H.; Kim, J.; Ihee, H. Cooperative Protein Structural Dynamics of Homodimeric Hemoglobin Linked to Water Cluster at Subunit Interface Revealed by Time-Resolved X-Ray Solution Scattering. *Struct. Dyn.* **2016**, *3*, 023610.
(49) Ren, Z.; Srajer, V.; Knapp, J. E.; Royer, W. E. Cooperative Macromolecular Device Revealed by Meta-Analysis of Static and Time-Resolved Structures. *Proc. Natl. Acad. Sci. U.S.A.* **2012**, *109*, 107−112.
(50) Knapp, J. E.; Pahl, R.; Srajer, V.; Royer, W. E. Allosteric Action in Real Time: Time-Resolved Crystallographic Studies of a Cooperative Dimeric Hemoglobin. *Proc. Natl. Acad. Sci. U.S.A.* **2006**, *103*, 7649−7654.
(51) Knapp, J. E.; Pahl, R.; Cohen, J.; Nichols, J. C.; Schulten, K.; Gibson, Q. H.; Srajer, V.; Royer, W. E. Ligand Migration and Cavities within Scapharca Dimeric Hbi: Studies by Time-Resolved Crystallography, Xe Binding, and Computational Analysis. *Structure* **2009**, *17*, 1494−1504.
(52) Zhou, Y.; Zhou, H.; Karplus, M. Cooperativity in Scapharca Dimeric Hemoglobin: Simulation of Binding Intermediates and Elucidation of the Role of Interfacial Water. *J. Mol. Biol.* **2003**, *326*, 593−606.
(53) Gupta, P. K.; Meuwly, M. Ligand and Interfacial Dynamics in a Homodimeric Hemoglobin. *Struct. Dyn.* **2016**, *3*, 012003.
(54) Pardanani, A.; Gambacurta, A.; Ascoli, F.; Royer, W. E. Mutational Destabilization of the Critical Interface Water Cluster in Scapharca Dimeric Hemoglobin: Structural Basis for Altered Allosteric Activity. *J. Mol. Biol.* **1998**, *284*, 729−739.
(55) Gnanasekaran, R.; Leitner, D. M. Dielectric Response and Vibrational Energy Relaxation in Photoactive Yellow Protein: A Molecular Dynamics Simulation Study. *Chem. Phys. Lett.* **2011**, *516*, 102−105.
(56) Royer, W. E. High-Resolution Crystallographic Analysis of a Co-Operative Dimeric Hemoglobin. *J. Mol. Biol.* **1994**, *235*, 657−681.
(57) Condon, P. J.; Royer, W. E. Crystal Structure of Oxygenated Scapharca Dimeric Hemoglobin at 1.7-a Resolution. *J. Biol. Chem.* **1994**, *269*, 25259−25267.
(58) Maier, J. A.; Martinez, C.; Kasavajhala, K.; Wickstrom, L.; Hauser, K. E.; Simmerling, C. Ff14sb: Improving the Accuracy of Protein Side Chain and Backbone Parameters from Ff99sb. *J. Chem. Theory Comput.* **2015**, *11*, 3696−3713.
(59) Jorgensen, W. L.; Chandrasekhar, J.; Madura, J. D.; Impey, R. W.; Klein, M. L. Comparison of Simple Potential Functions for Simulating Liquid Water. *J. Chem. Phys.* **1983**, *79*, 926−935.
(60) Price, D. J.; Brooks, C. L. A Modified Tip3p Water Potential for Simulation with Ewald Summation. *J. Chem. Phys.* **2004**, *121*, 10096−10103.
(61) Case, D. A.; Cheatham, T. E.; Darden, T.; Gohlke, H.; Luo, R.; Merz, K. M.; Onufriev, A.; Simmerling, C.; Wang, B.; Woods, R. J. The Amber Biomolecular Simulation Programs. *J. Comput. Chem.* **2005**, *26*, 1668−1688.
(62) Case, D. A.; Betz, R. M.; Cerutti, D. S.; Cheatham, T. E.; Darden, T. A.; Duke, R. E.; Giese, T. J.; Gohlke, H.; Goetz, A. W.; Homeyer, N.; et al. *Amber 2016*; University of California: San Francisco, 2016.
(63) Frisch, M. J.; Trucks, G. W.; Schlegel, H. B.; Scuseria, G. E.; Robb, M. A.; Cheeseman, J. R.; Montgomery, J. A.; Vreven, T.; Kudin, K. N.; Burant, J. C.; et al. *Gaussian 16*, Revision 16; Gaussian, Inc.: Wallingford CT: 2016.

https://dx.doi.org/10.1021/acs.jpcb.9b11413
J. Phys. Chem. B 2020, 124, 1148−1159

(64) Singh, U. C.; Kollman, P. A. An Approach to Computing Electrostatic Charges for Molecules. *J. Comput. Chem.* **1984**, *5*, 129−145.
(65) Lu, T.; Chen, F. Multiwfn: A Multifunctional Wavefunction Analyzer. *J. Comput. Chem.* **2012**, *33*, 580−592.
(66) Shahrokh, K.; Orendt, A.; Yost, G. S.; Cheatham, T. E. Quantum Mechanically Derived Amber-Compatible Heme Parameters for Various States of the Cytochrome P450 Catalytic Cycle. *J. Comput. Chem.* **2012**, *33*, 119−133.
(67) Pettersen, E. F.; Goddard, T. D.; Huang, C. C.; Couch, G. S.; Greenblatt, D. M.; Meng, E. C.; Ferrin, T. E. Ucsf Chimera-a Visualization System for Exploratory Research and Analysis. *J. Comput. Chem.* **2004**, *25*, 1605−1612.
(68) Webb, B.; Sali, A. Comparative Protein Structure Modeling Using Modeller. *Current Protocols in Bioinformatics*; John Wiley & Sons, Inc.: Hoboken, NJ, USA, 2016; Vol. *176*, pp 5.6.1−5.6.37.
(69) Berendsen, H. J. C.; Postma, J. P. M.; van Gunsteren, W. F.; DiNola, A.; Haak, J. R. Molecular Dynamics with Coupling to an External Bath. *J. Chem. Phys.* **1984**, *81*, 3684−3690.
(70) Yamato, T. Energy Flow Pathways in Photoreceptor Proteins. In *Proteins: Energy, Heat and Signal Flow*; Leitner, D. M., Straub, J. E., Eds.; CRC Press, Taylor and Francis Group: Boca Raton, 2010; pp 129−147.
(71) Nakayama, T.; Yakubo, K.; Orbach, R. L. Dynamical Properties of Fractal Networks: Scaling, Numerical Simulations, and Physical Realizations. *Rev. Mod. Phys.* **1994**, *66*, 381−443.
(72) Alexander, S.; Orbach, R. Density of States on Fractals: "Fractons". *J. Phys. Lett.* **1982**, *43*, 625−631.
(73) Alexander, S.; Bernasconi, J.; Schneider, W. R.; Orbach, R. Excitation Dynamics in Random One-Dimensional Systems. *Rev. Mod. Phys.* **1981**, *53*, 175−198.
(74) Rammal, R.; Toulouse, G. Random Walks on Fractal Structures and Percolation Clusters. *J. Phys. Lett.* **1983**, *44*, 13−22.
(75) Yu, X.; Leitner, D. M. Anomalous Diffusion of Vibrational Energy in Proteins. *J. Chem. Phys.* **2003**, *119*, 12673−12679.
(76) Enright, M. B.; Yu, X.; Leitner, D. M. Hydration Dependence of the Mass Fractal Dimension and Anomalous Diffusion of Vibrational Energy in Proteins. *Phys. Rev. E: Stat., Nonlinear, Soft Matter Phys.* **2006**, *73*, 051905.
(77) Enright, M. B.; Leitner, D. M. Mass Fractal Dimension and the Compactness of Proteins. *Phys. Rev. E: Stat., Nonlinear, Soft Matter Phys.* **2005**, *71*, 011912.
(78) Sethi, A.; Eargle, J.; Black, A. A.; Luthey-Schulten, Z. Dynamical Networks in tRNA:Protein Complexes. *Proc. Natl. Acad. Sci. U.S.A.* **2009**, *106*, 6620−6625.
(79) Lee, Y.; Choi, S.; Hyeon, C. Mapping the Intramolecular Signal Tranduction of G-Protein Coupled Receptors. *Proteins: Struct., Funct., Bioinf.* **2014**, *82*, 727−743.
(80) Thirumalai, D.; Hyeon, C. Signalling Networks and Dynamics of Allosteric Transitions in Bacterial Chaperonin Groel: Implications for Iterative Annealing of Misfolded Proteins. *Philos. Trans. R. Soc., B* **2018**, *373*, 20170182.
(81) Achoch, M.; Dorantes-Gilardi, R.; Wymant, C.; Feverati, G.; Salamatian, K.; Vuillon, L.; Lesieur, C. Protein Structural Robustness to Mutations: An in Silico Investigation. *Phys. Chem. Chem. Phys.* **2016**, *18*, 13770−13780.
(82) Vuillon, L.; Lesieur, C. From Local to Global Changes in Proteins: A Network View. *Curr. Opin. Struct. Biol.* **2015**, *31*, 1−8.
(83) Gheeraert, A.; Pacini, L.; Batista, V. S.; Vuillon, L.; Lesieur, C.; Rivalta, I. Exploring Allosteric Pathways of a V-Type Enzyme with Dynamical Perturbation Networks. *J. Phys. Chem. B* **2019**, *123*, 3452−3461.
(84) Livi, L.; Maiorino, E.; Pinna, A.; Sadeghian, A.; Rizzi, A.; Giuliani, A. Analysis of Heat Kernel Highlights the Strongly Modular and Heat-Preserving Structure of Proteins. *Phys. A* **2016**, *441*, 199−214.
(85) Di Paola, L.; Giuliani, A. Protein Contact Network Topology: A Natural Language for Allostery. *Curr. Opin. Struct. Biol.* **2015**, *31*, 43−48.
(86) Livi, L.; Maiorino, E.; Giuliani, A.; Rizzi, A.; Sadeghian, A. A Generative Model for Protein Contact Networks. *J. Biomol. Struct. Dyn.* **2016**, *34*, 1441−1454.
(87) Di Paola, L.; De Ruvo, M.; Paci, P.; Santoni, D.; Giuliani, A. Protein Contact Networks: An Emerging Paradigm in Chemistry. *Chem. Rev.* **2013**, *113*, 1598−1613.
(88) Lu, C.; Knecht, V.; Stock, G. Long-Range Conformational Response of a PDZ Domain to Ligand Binding and Release: A Molecular Dynamics Study. *J. Chem. Theory Comput.* **2016**, *12*, 870−878.
(89) Gulzar, A.; Valiño Borau, L.; Buchenberg, S.; Wolf, S.; Stock, G. Energy Transport Pathways in Proteins: A Non-equilibrium Molecular Dynamics Simulation Study. *J. Chem. Theory Comput.* **2019**, *15*, 5750−5757.
(90) Buchenberg, S.; Knecht, V.; Walser, R.; Hamm, P.; Stock, G. Long-Range Conformational Transition of a Photoswitchable Allosteric Protein: Molecular Dynamics Simulation Study. *J. Phys. Chem. B* **2014**, *118*, 13468−13476.
(91) Smock, R. G.; Gierasch, L. M. Sending Signals Dynamically. *Science* **2009**, *324*, 198−203.
(92) Buchli, B.; Waldauer, S. A.; Walser, R.; Donten, M. L.; Pfister, R.; Blochliger, N.; Steiner, S.; Caflisch, A.; Zerbe, O.; Hamm, P. Kinetic Response of a Photoperturbed Allosteric Protein. *Proc. Natl. Acad. Sci. U.S.A.* **2013**, *110*, 11725−11730.
(93) Stock, G.; Hamm, P. A Nonequilibrium Approach to Allosteric Communication. *Philos. Trans. R. Soc., B* **2018**, *373*, 20170187.

https://dx.doi.org/10.1021/acs.jpcb.9b11413
J. Phys. Chem. B 2020, 124, 1148−1159